Article

Chirality-transferred epitaxy of circular polarization-sensitive ReS$_2$ monolayer single crystals

Check for updates

Junjie Jiang[1,2,3,12], Xiao Wang [4,12], Danyang Wang[2,12], Yue Chai[5], Yue Yang[5], Lingtong Ding[4], Xiao Guo[3], Aolin Li[6], Tao Xu[3], Han Huang [3], Shen Zhou [7], Zheng Luo[2], Jin Zhang [1], Fangping Ouyang [3,6,8] ✉, Feng Ding [4,9,10] ✉, Zhu-Jun Wang [5] ✉ & Shanshan Wang [1,2,11] ✉

The epitaxial growth of semiconducting two-dimensional (2D) materials is vital to achieve wafer-scale single-crystalline films for beyond-silicon electronics. However, gaining full control over both in-plane and out-of-plane orientations (i.e., lateral crystal alignments and chirality) is particularly challenging when growing low-symmetry 2D single crystals. Here, using triclinic ReS$_2$ semiconductor monolayers as a model system, we demonstrate the chirality-controlled epitaxial growth of unidirectional, anisotropic single crystals on an insulating chiral surface via the synergy of terraces, steps, and kinks, yielding >97.5% chirality selectivity and >99% in-plane orientation consistency. The products display an anisotropic ratio of 1.9 in photodetection (comparable to exfoliated samples) and high distinguishability of circularly polarized light. Theoretical calculations combined with a set of microscopy and spectroscopy methods show that terrace facets determine the epitaxial growth direction, while steps and kinks break the degeneracy of ReS$_2$ in the lateral orientation and chirality. This approach is also applicable to the chiral epitaxy of other low-symmetry 2D single crystals, like monoclinic MoO$_2$. Our method extends the range of control over 2D material growth, enabling chirality transfer from the substrate to the crystal, and promotes the large-area synthesis of chirality-selected, single-crystal 2D materials.

The epitaxial growth of two-dimensional (2D) materials is a promising route to wafer-scale, single-crystalline, atomically thin films, showing great potential in integrated electronic and optoelectronic devices beyond silicon[1–4]. Substrate engineering plays a crucial role in realizing this goal. For monolayer growth, methods like introducing step edges[5–9], defects[10,11], and interfacial reconstructed layers[12,13], as well as selecting appropriate substrate surface symmetry[14–16], have been utilized to prepare graphene, hexagonal boron nitride, 2H-MoSe$_2$, and 2H-WSe$_2$. For multilayers, techniques like bevel-edge epitaxy[17], interfacial epitaxy[18], and remote epitaxy[19] have been applied to control interfacial stacking order and thickness for rhombohedral boron nitride, 2H-MoS$_2$, and 2H-WS$_2$. However, most of these 2D materials are high-symmetry crystals (e.g., graphene: C_{6v}; h-BN: C_{3v}; 2H-MoS$_2$, −MoS$_2$, −WS$_2$, and −WSe$_2$: D_{3h}), while low-symmetry ones such as triclinic ReX$_2$ (X = S, Se) and monoclinic 1T'-MTe$_2$ (M = Mo, W) receive limited attention in epitaxial 2D fabrication studies. These low-symmetry 2D layers require more stringent control of the lattice orientation than the high-symmetry crystals even for monolayers due to the following reasons.

Firstly, low-symmetry crystal structures lead to abundant in-plane anisotropic properties, which can only be effectively manifested at the

macroscopic scale when the 2D material adopts a single lateral lattice orientation across a wide range. The presence of different orientated domains results in grain boundaries (GBs) that degrade carrier mobility and spatially averages out the anisotropic properties of low-symmetry crystals, ultimately impacting mechanical, electronic, and optical applications. Efforts have been devoted to the in-plane orientation-controlled epitaxial growth via substrate engineering[20–24]. Take ReS$_2$ (P$\bar{1}$) as an example, which is a typical low-symmetry semiconducting 2D material possessing only an inversion center as the symmetric element, monolayer single-crystalline ReS$_2$ domains with unidirectionally aligned **b**-axis (orientation of Re4 chains) were grown on Au(101) due to strong interfacial coupling and low-symmetry of the substrate surface (C_{2v})[23]. More recently, continuous 2D ReS$_2$ films with a consistent **b**-axis orientation were achieved on Au(111) by introducing step edges along $[01\bar{1}]$ to decrease the surface symmetry to C_s (having a mirror plane)[24]. However, these approaches suffer from high substrate cost (noble metal), limited crystal quality, non-uniform thickness, and, more importantly, the inability to control the out-of-plane lattice orientation of monolayers, which will result in the achievement of racemic mixture rather than a single structure (discussed in the next paragraph).

The necessity to control orientations of low-symmetry 2D crystals comes from an even more important reason, i.e., monolayers with opposite vertical lattice directions have different chirality in two dimensions when they are confined to a plane, meaning that they cannot be interconverted by any rotation about the axis perpendicular to the substrate. This is illustrated by monolayer ReS$_2$ in Fig. 1a. R-ReS$_2$ and S-ReS$_2$ are enantiomers, despite having the same in-plane **b**-axis orientation (Re4 chain direction marked in red), and they display exotic physical properties like chiral Raman scattering[25,26]. In other words, when monolayer ReS$_2$, which is achiral in three dimensions, binds to a substrate, its original inversion center disappears, thus generating a chiral ReS$_2$/substrate interface in space. This phenomenon introduces an additional degree of freedom for structural control of low-symmetry 2D crystals, expanding the possibility for performance tuning but also increasing the difficulty of material fabrication. Currently, the construction of chiral 2D structures predominantly focuses on twisted-stacked 2D crystals via sequential mechanical transfer and screw dislocation-triggered growth[27–30], layered 2D crystals intercalated by chiral molecules[31], and chiral perovskites via direct synthesis[32,33], among which diversified chirality-dependent exotic properties like spin selectivity, magnetic phases, and photoelectric responses were discovered[33–35]. Yet chirality-selected growth of low-symmetry monolayer single crystals by complete control over both in-plane and out-of-plane lattice orientations is blank and urgently needed.

Herein, we demonstrate the chemical vapor deposition (CVD) growth of chirality-selected unidirectionally aligned monolayer ReS$_2$ single crystals on a cost-effective and industry-compatible insulating substrate via a terrace-step-kink strategy. The acquisition of the target material is decomposed into three steps with correspondingly developed substrate engineering methods (Fig. 1e–g). Step 1: Realizing the single-crystallinity of each ReS$_2$ domain, fulfilled by choosing the substrate terrace facet with an appropriate rotation symmetry, which can prohibit ReS$_2$ from generating thermodynamically favorable GBs during the epitaxial growth (Fig. 1e). Step 2: Realizing the in-plane unidirectional alignment of every single-crystalline domain, reached by introducing specific steps on the terrace (Fig. 1f), thus breaking the binding energy degeneracy of differently oriented ReS$_2$ domains. Step 3: Realizing the chirality selectivity of unidirectionally aligned single crystals. A chiral substrate surface was constructed by further introducing selected kinks to the "terrace + step" microstructures (Fig. 1g) so that a chirality transfer mechanism functions, which enables breaking both interfacial configuration and energy degeneracy of monolayer single-crystalline ReS$_2$ enantiomers (definitions of steps and kinks are included in Supplementary Fig. 1).

Results

Terrace-step-kink strategy of substrate design

Considering crystal structure, physical properties, and material costs, MgO, a binary cubic system with high chemical and thermal stability, was selected as the substrate. Its insulating characteristic also facilitates better compatibility of the 2D semiconducting materials grown on it with the current integrated circuit technology. Firstly, we performed DFT calculations to verify the theoretical feasibility of the above substrate design strategy. The key to achieving single-crystalline ReS$_2$ domains (Step 1) is to prevent Re4 chains from deflecting during growth and forming GBs. Previous literature has demonstrated that, distinct from 2D materials like MoS$_2$ and WS$_2$ which can spontaneously grow into triangular/hexagonal single crystals under most conditions, Re4 chains in ReS$_2$ are prone to deflect integer multiples of ~60° during domain growth, thereby generating a series of highly coherent GBs with low formation energies and leading to polycrystalline products[36–38]. Therefore, we chose MgO(001) with C_{4v} as the substrate terrace facet rather than α-Al$_2$O$_3$(0001) (C_{3v}) and mica(0001) (C_{6v}) in order to prohibit ReS$_2$ from generating thermodynamically advantageous GBs when epitaxially grown on the single-crystalline substrate. Theoretical calculations exhibit that monolayer ReS$_2$ single crystals have two optimal epitaxial growth orientations orthogonal to each other on MgO(001), whose intersectional angles (θ) between the **b**-axis of ReS$_2$ and MgO[110] is 0° and 90°, respectively. The suboptimal epitaxial orientation is $\theta = 45°$ (Fig. 1h and Supplementary Fig. 2). On the premise of ensuring a superior epitaxial growth orientation on the substrate, monolayer ReS$_2$ can only construct GBs with inter-grain angles of 45° and 90°, whose calculated formation energies are significantly larger than those highly coherent GBs commonly observed in previous work[38] (e.g., the GB with an inter-grain angle of 120°, Fig. 1i). It indicates thermodynamic prohibition to form GBs for epitaxially grown ReS$_2$ single layers on MgO(001) with C_{4v} symmetry.

To achieve unidirectional alignment of single-crystalline domains (Step 2), we introduced steps along the crystallographic orientation of $[\bar{1}10]$ (named step$[\bar{1}10]$) on the terrace(001) of MgO. Such surface microstructures, in principle, can be obtained by spontaneous reconstruction of the vicinal MgO(001), referred to as MgO(11l) ($l \gg 1$), after annealing (Fig. 1b). It is noteworthy that the step orientation was deliberately designed to be parallel with and perpendicular to the **b**-axis orientations of two orthogonally oriented ReS$_2$ single crystals epitaxially grown on the terrace(001). This design can maximize the interfacial structural disparity of two oriented ReS$_2$ single crystals on the substrate and break energy degeneracy remarkably. DFT calculations show a prominently lower interfacial binding energy when the **b**-axis direction of ReS$_2$ is parallel with step$[\bar{1}10]$ on MgO than when they are perpendicular (Fig. 1j), implying that introducing step$[\bar{1}10]$ can thermodynamically drive uniform orientation of monolayer ReS$_2$ single crystals. It is worth noting that since the reconstructed MgO(11l) still has mirror symmetry (C_s), the structures of ReS$_2$ enantiomers on the substrate surface mirror each other (Supplementary Fig. 3), displaying the same manner of interfacial atomic alignment and thus degenerated binding energies. Therefore, chirality selectivity is incapable of being realized solely by the "terrace(001) + step$[\bar{1}10]$" substrate design.

Finally, we introduced kinks along lattice directions of $[\bar{1}00]$ and [010] (named kink$[\bar{1}00]$ and kink[010]) on the MgO surface involving terrace(001) and step$[\bar{1}10]$. Such design eliminates the mirror symmetry of the substrate, thus constructing chiral surfaces which may realize chirality-selective growth (Step 3, Fig. 1c, d and Supplementary Fig. 4). The chiral surfaces can commonly be obtained by thermal treatment of MgO(12l) and MgO(21l) ($l \geq 2$) because unstable high-index facets are inclined to reconstruct to thermodynamically
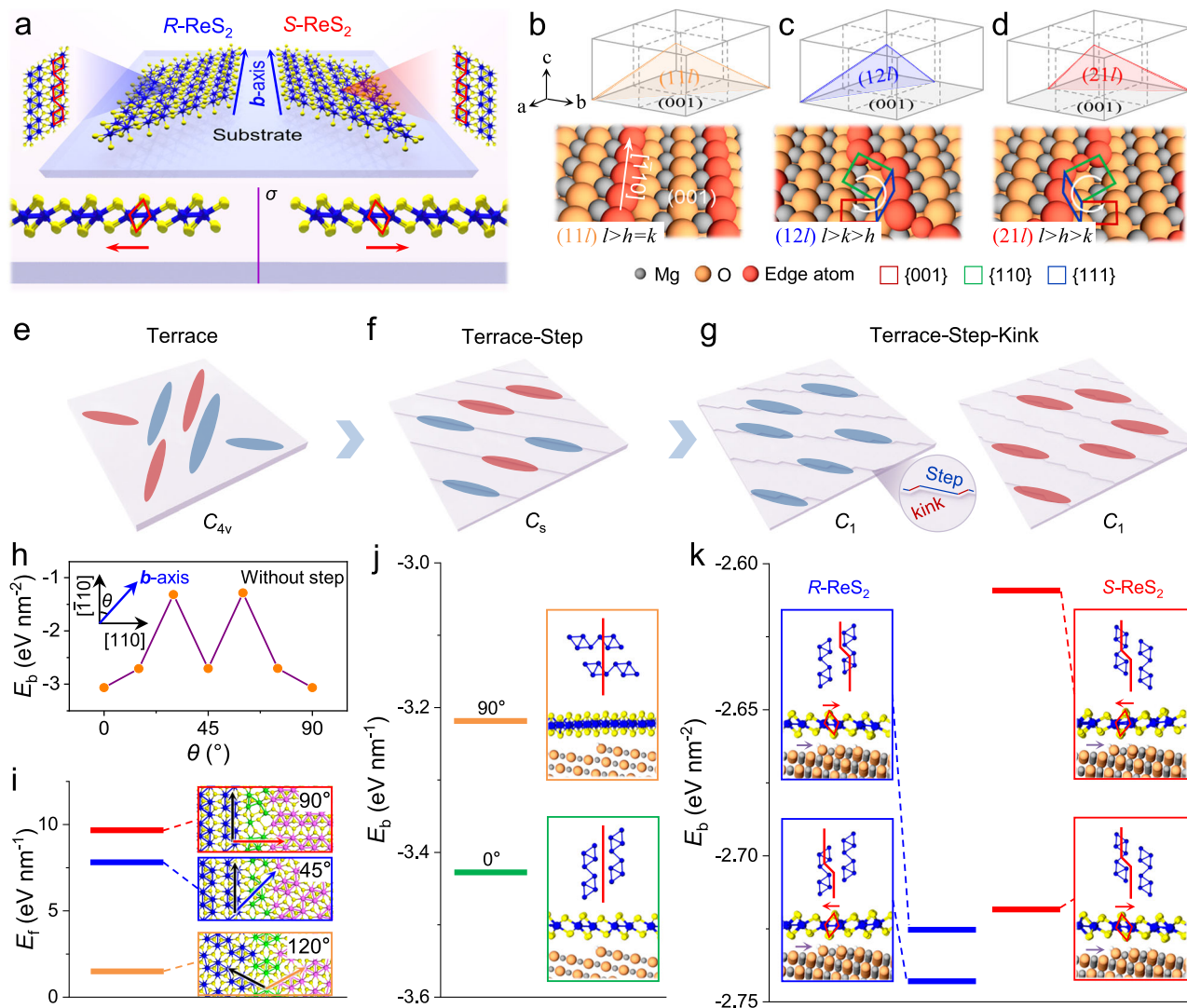
Fig. 1 | Terrace-step-kink strategy of substrate design. a Schematic illustrating chirality of monolayer ReS$_2$ on the substrate, where R and S refer to rectus and sinister in Latin, respectively, representing two types of enantiomers. The structural differences between R- and S-ReS$_2$ on the substrate surface are marked by red symbols. **b–d** Schematics showing the substrate surface reconstruction from MgO(11l) to terrace facets (001) with bunched steps along [$\bar{1}$10] (**b**) and reconstruction from chiral surface R-(12l)/S-(21l) to terrace facets (001) with bunched steps along [$\bar{1}$10] and kinks along [$\bar{1}$00]/[010] (**c** and **d**). **e–g** Scheme of the designed terrace-step-kink strategy, which gradually increases the structural selectivity of the as-grown ReS$_2$ on the MgO substrate by sequentially introducing specific terraces, steps, and kinks to the reconstructed substrate surfaces to reduce their structural symmetry, thus eliminating energy degeneracy of monolayer ReS$_2$ single crystals with different orientations and chirality. Blue and red blocks represent ReS$_2$ domains in different chirality. The gray lines represent microstructures on the reconstructed substrate surfaces with the zoomed-in inset highlighting steps and kinks. **h** Binding energies (E_b) calculated using density functional theory (DFT) for ReS$_2$ single-crystalline domains with different rotation angles (θ) on MgO(001), θ represents the angle between the b-axis ([010]) of ReS$_2$ and MgO [$\bar{1}$10]. **i** Formation energies (E_f) of three grain boundaries with different inter-grain twist angles (insets). **j** Binding energies (E_b) of monolayer single-crystalline ReS$_2$ domains oriented perpendicularly on reconstructed MgO(11l) composed of terrace(001) and step[$\bar{1}$10]. The red lines in the top panel of the insets represent step[$\bar{1}$10] on the reconstructed MgO surface, while the blue rhombuses represent Re4 chains of monolayer ReS$_2$. **k** Binding energies (E_b) of R- and S-ReS$_2$ monolayer single crystals with the same b-axis orientation on the chiral reconstructed MgO(12l)^R surface. The red curves (top panels in the insets) represent the "step + kink" configuration on MgO.

favorable low-index counterparts. By definition, (12l) and (21l) can be assigned to rectus (R) and sinister (S) configurations, which are termed (12l)^R and (12l)^S ($l \gg 2$), respectively (Supplementary Fig. 5). It is noteworthy that the construction of chiral surfaces only requires (hkl) to satisfy $h \neq k \neq l$ and $h \times k \times l \neq 0$ geometrically. Here, we designed chiral surfaces of (12l)^R and (12l)^S ($l \gg 2$) for the following reasons: (i) Selection of high-index planes with $l \gg 2$ ensures a sufficiently large area of each terrace layer and a low height of every step/kink after surface reconstruction, which facilitate monolayer nucleation and rapid domain expansion across steps/kinks. (ii) Reconstructed surfaces of (12l)^R and (12l)^S have a similar density of step[$\bar{1}$10] to that of the reconstructed (11l) designed in Step 2. Moreover, the length of the newly introduced kink[$\bar{1}$10]/kink[010] is $1/\sqrt{2} \approx 70\%$ of the step[$\bar{1}$10] length. Such design

allows the substrate to effectively control both the in-plane alignment and chirality of ReS$_2$ single crystals. DFT calculations display that the binding energy of R-ReS$_2$ on MgO(12l)^R is lower than that of S-ReS$_2$ on MgO(12l)^R (Fig. 1k), suggesting chirality transfer from the substrate surface to the as-grown monolayer products.

Growth of chirality-selected, unidirectional ReS$_2$ single crystals

Experimentally, the chiral substrate (e.g., (12l)^S) was achieved by custom-designing MgO(001) with a cutting angle of ~1° towards [210] (Supplementary Figs. 6 and 7). The surface was reconstructed into terraces(001) with a bunch of parallelly aligned steps along [$\bar{1}$20] (Supplementary Fig. 8) after annealing in oxygen. These steps are, in principle, composed of step[$\bar{1}$10] and kink[010] at the nanometer scale
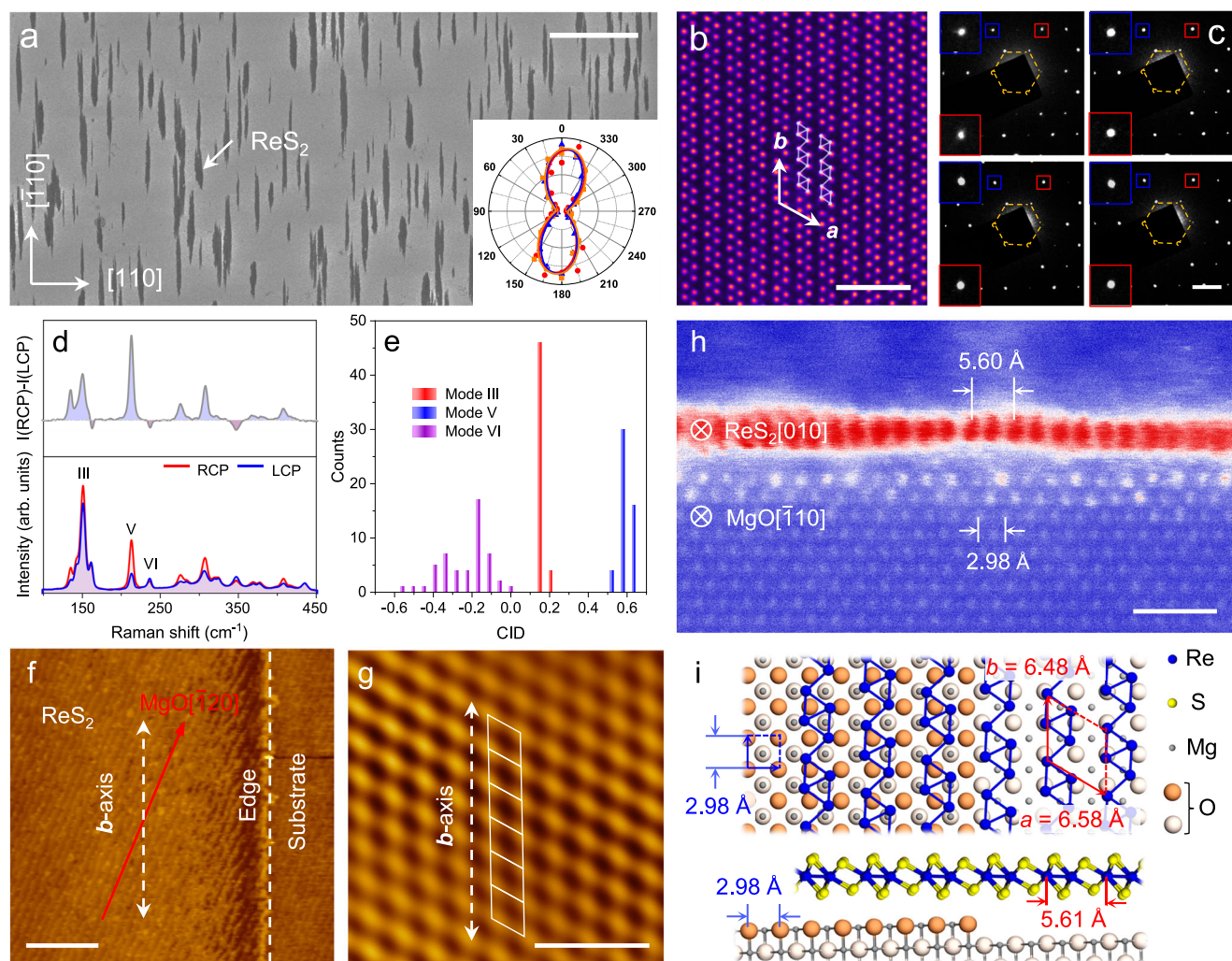
Fig. 2 | Growth and characterization of chirality-selected, unidirectional, single-crystalline monolayer ReS₂. Wait.

Fig. 2 | Growth and characterization of chirality-selected, unidirectional, single-crystalline monolayer ReS_2. **a** Scanning electron microscopy (SEM) image of unidirectionally aligned spindle-like ReS_2 domains grown on $MgO(12l)^S$. The inset shows the angle-resolved Raman intensities of the vibrational mode of ReS_2 at 212 cm⁻¹ captured at three different locations in one domain. Scale bar: 20 μm. **b** Annular dark-field scanning transmission electron microscopy (ADF-STEM) image of monolayer ReS_2. The Re4 chains are represented by white rhombuses with crystallographic directions a [100] and b [010] labeled. Scale bar: 2 nm. **c** Selected area electron diffraction (SAED) patterns obtained at four different domains. The yellow hexagons mark the innermost diffraction spots, while the insets are the zoomed-in views of the red- and blue-boxed high-index diffraction spots. Scale bar: 2 nm⁻¹. **d** Circularly polarized Raman (CPR) spectra of as-grown ReS_2 in (**a**) (bottom) and the difference between the Raman intensities excited by right-handed (RCP) and left-handed (LCP) circularly polarized light (top). The wavelength of the polarized light is 532 nm. **e** Histogram showing the circular intensity difference (CID) distribution of Raman modes III (153 cm⁻¹), V (212 cm⁻¹), and VI (235 cm⁻¹) captured from ≈50 ReS_2 domains located at different regions on $MgO(12l)^S$. **f** Atomic force microscopy (AFM) image displaying a ReS_2 domain (left to the white dashed line) grown on bare $MgO(12l)^S$ (right to the white dashed line). The reconstructed steps along $MgO[\bar{1}20]$ (which are composed of step $[\bar{1}10]$ and kink $[010]$ at the atomic scale) are marked by the red arrow, while the b-axis of ReS_2 is labeled by the white arrow. Scale bar: 200 nm. **g**, Zoomed-in atomically resolved AFM image of the ReS_2 domain in (**f**). The Re rhombic lattice along the b-axis is marked by white lines. Scale bar: 2 nm. **h** Cross-sectional ADF-STEM image of the ReS_2/MgO interface viewed along $MgO[\bar{1}10]$. Scale bar: 1 nm. **i** Schematic illustrating the epitaxial relationship of monolayer ReS_2 on reconstructed $MgO(12l)^S$. The orange and white spheres represent the first and second layers of O atoms of the MgO surface, respectively.

(Fig. 1d). Figure 2a shows spindle-shaped ReS_2 crystals with a length of 15−20 μm grown on $MgO(12l)^S$ by hydrogen-free atmospheric-pressure CVD. They were unidirectionally aligned along $MgO[\bar{1}10]$ and can merge together with atomically stitched interfaces (Supplementary Fig. 9). The angle-dependent Raman intensities of the vibrational mode at 212 cm⁻¹ were measured in the parallel polarization configuration for different crystals and various locations in the same crystal of the as-grown ReS_2 (inset of Fig. 2a and Supplementary Fig. 10). They exhibited almost overlapped double-lobed patterns with the maximized intensity corresponding to an angle of 353° ± 4° (0° in the polar plot corresponded to the major axis direction of the spindle-like domain), indicating that the as-prepared products have consistent crystallographic orientation within and between crystals and the major axis

direction of the spindle-shaped crystals corresponds to the b-axis orientation of ReS_2. The second harmonic generation (SHG) spectra and mapping further verified single-crystallinity without GBs of ReS_2 grown on $MgO(12l)^S$ because no obvious signal was detected, which was in stark contrast to the strong SHG intensity observed in polycrystalline ReS_2 prepared on α-Al_2O_3(0001) (Supplementary Figs. 11 and 12). Annular dark-field scanning transmission electron microscopy (ADF-STEM) showed well-organized Re4 chains with neither detectable lattice deformation nor atom missing, demonstrating monolayer thickness of the 2D products with superior crystal quality at the atomic scale (Fig. 2b). Selected area electron diffraction (SAED) captured at different domains displayed only one set of quasi-hexagonal patterns aligning in the same orientation without high-

order diffraction spots splitting (Fig. 2c), manifesting consistent lattice orientation of disparate domains (Supplementary Fig. 13).

We then applied CPR spectroscopy to determine the 2D chirality of ReS$_2$ on MgO(12l)^S. Remarkable differences in relative intensities were observed in CPR spectra of as-grown domains under RCP and LCP due to phase differences among multiple phonon-mediated electron scattering pathways[25] (Fig. 2d). The CID values, defined as $(I_{RCP} - I_{LCP}) / (I_{RCP} + I_{LCP})$, for vibrational mode III (151 cm^{-1}), V (212 cm^{-1}), and VI (235 cm^{-1}) were measured to be 0.124, 0.523, and −0.214, respectively, agreeing well with those for S-ReS$_2$. We characterized CPR spectra from 50 randomly selected ReS$_2$ domains grown at various positions on MgO(12l)^S. The statistical results demonstrated that the CID feature exhibited in Fig. 2d was universal, implying S chiral configuration enrichment of our sample (Fig. 2e).

Atomic force microscopy (AFM) and cross-sectional ADF-STEM were employed to unveil the epitaxial relationship between ReS$_2$ and MgO(12l)^S. The b-axis direction of monolayer ReS$_2$ was found to deflect ∼18.5° from parallelly aligned edges along $[\bar{1}20]$ on reconstructed MgO(12l)^S in the AFM image (Fig. 2f, g and Supplementary Fig. 14), proving again that the major axis (b-axis) of the spindle-shaped ReS$_2$ crystals is parallel to MgO$[\bar{1}10]$ rather than MgO$[\bar{1}20]$. The cross-sectional ADF-STEM image displayed the atomic arrangement of monolayer S-ReS$_2$ on MgO along MgO$[\bar{1}10]$ (Fig. 2h). The lattice spacing of ReS$_2$ in the lateral direction was measured as 5.60 Å, well matching with $a_{ReS_2} \times \sin \alpha_{ReS_2} = 5.61$ Å ($a_{ReS_2} = 6.58$ Å, $\alpha_{ReS_2} = 121.5°$ representing the angle between a-axis and b-axis of ReS$_2$), which corresponds to the lattice spacing of ReS$_2$ perpendicular to its b-axis direction. The lattice spacing of MgO was measured as 2.98 Å, consistent with $\sqrt{2}a_{MgO}/2 = 2.98$ Å ($a_{MgO} = 4.21$ Å). These results directly confirmed that the (001) lattice plane of ReS$_2$ is parallel to the (001) terrace facet of MgO and the b-axis of ReS$_2$ is parallel to the $[\bar{1}10]$ lattice direction of MgO, which can be expressed as [010]ReS$_{2(001)}$// $[\bar{1}10]$MgO$_{(001)}$ (Fig. 2i). In addition, the atomic step on the reconstructed substrate showed a height of ∼2.14 Å corresponding to half the lattice constant of MgO ($a_{MgO}/2 = 2.16$ Å), and ReS$_2$ was observed to grow across steps (Supplementary Fig. 15). The distance between ReS$_2$ and the MgO step edge (2.75 Å) is close to the van der Waals gap between ReS$_2$ and the MgO terrace (3.10 Å), suggesting van der Waals coupling at the ReS$_2$/MgO step edge interface. These characteristics indicate that the terrace facets of MgO determine the epitaxial orientation of monolayer ReS$_2$, while the steps/kinks are used to break the energy degeneracy of ReS$_2$ with different lattice directions to achieve full structural control. The terrace-step-kink strategy can also be extended to the chirality-selective growth of other unidirectional low-symmetry 2D single crystals, such as monoclinic MoO$_2$ (Supplementary Fig. 16).
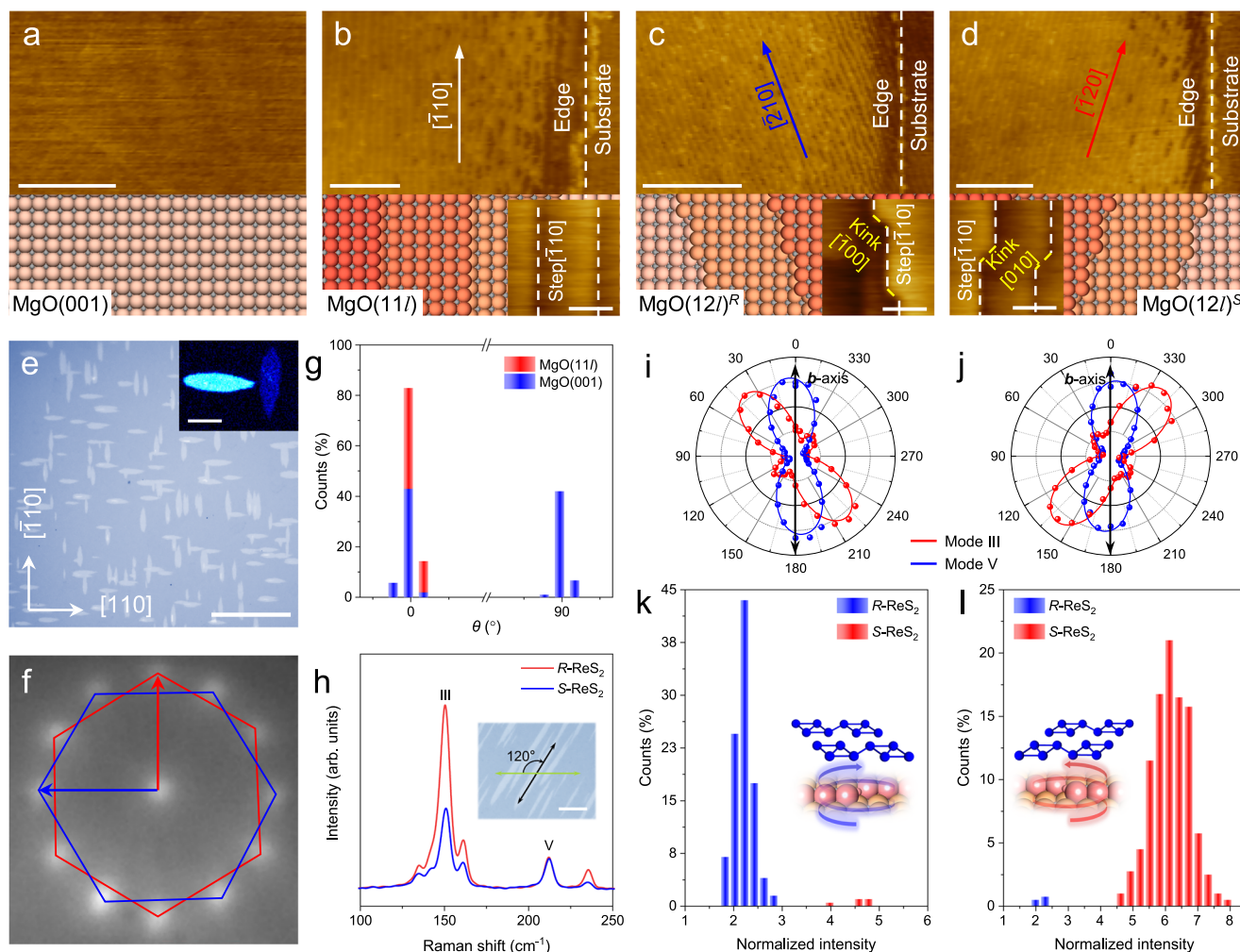
Structural selectivity improvement by substrate engineering

To achieve an in-depth comprehension of how terraces, steps, and kinks on MgO control the structure of monolayer ReS$_2$ and validate the theoretical calculations in Fig. 1, we compared the growth results of ReS$_2$ on MgO(001), MgO(11l), and chiral surfaces of MgO(12l)^R and MgO(12l)^S, respectively. On the flat MgO(001) without steps and kinks (Fig. 3a), the contrast under a polarized optical microscope and the angle-resolved Raman intensity mapping at 212 cm^{-1} displayed homogeneous brightness in each crystal (inset of Fig. 3e and Supplementary Figs. 17 and 18), indicating the achievement of single-crystalline ReS$_2$ domains on MgO(001) with C_{4v} symmetry. However, two epitaxial growth orientations of ReS$_2$ crystals along [110] and $[\bar{1}10]$ of MgO, respectively, were observed, which were evidenced by the optical microscopy (OM) image and the sharp intensity disparity between two orthogonally oriented ReS$_2$ crystals in the angle-resolved Raman mapping (Fig. 3e). Moreover, twelve spots which can be assigned to two sets of quasi-hexagonal patterns perpendicular to each other were obtained when conducting low-energy electron diffraction (LEED) on

the as-grown ReS$_2$ (Fig. 3f), further demonstrating the incapability of realizing unidirectional alignment of ReS$_2$ single crystals on MgO(001).

We then cut MgO(001) towards [110] with an angle of ∼1° to achieve MgO(11l). The substrate surface was reconstructed to straight, low-index atomic steps arranged parallel to $[\bar{1}10]$ after annealing (Fig. 3b). OM and angle-resolved polarization Raman spectroscopy showed that the introduction of step$[\bar{1}10]$ on MgO(001) led to unidirectional alignment of spindle-shaped ReS$_2$ single crystals with an orientation selectivity of >99% (red columns in Fig. 3g and Supplementary Fig. 19). In contrast, on MgO(001), the ratio of ReS$_2$ domains aligning along [110] and $[\bar{1}10]$ was 49:51 (blue columns in Fig. 3g), demonstrating the decisive role of step$[\bar{1}10]$ in breaking the symmetry of the orthogonal orientations of ReS$_2$ single crystals. Next, we applied a method to rapidly identify the chiral configuration of the 2D products by comparing the Raman peak intensity between the chirality-sensitive mode III (151 cm^{-1}) and chirality-insensitive mode V (212 cm^{-1}), which was measured by setting an angle ($\varphi = 120°$) between the linear polarization direction of the incident laser and the b-axis of ReS$_2$ (Fig. 3h, details discussed in the next paragraph and Supplementary Fig. 20). The statistics captured from 100 showed that the quantity ratio of S- and R-ReS$_2$ was 43:57 (Supplementary Fig. 21), implying that solely introducing step$[\bar{1}10]$ on terrace(001) cannot reach chirality selectivity of monolayer ReS$_2$.

Finally, the chiral surfaces of MgO(12l)^R and MgO(12l)^S were applied to prepare monolayer ReS$_2$. Well-organized step edges along $[\bar{2}10]$ and $[\bar{1}20]$ were displayed on the reconstructed chiral surfaces after annealing (top panels in Fig. 3c, d), which exhibited jagged edges composed of low-index step$[\bar{1}10]$ and kink$[\bar{1}00]$/kink[010] at the nanometer scale (bottom panels in Fig. 3c, d). Since Fig. 2 has included comprehensive characterization of the single-crystallinity, orientation consistency, and epitaxial relationship of monolayer ReS$_2$ on MgO(12l)^S and utilized CID to demonstrate the single chirality of the 2D products qualitatively, here we focused on the quantitative analysis of the chirality selectivity of monolayer ReS$_2$ crystals grown on R and S chiral MgO surfaces from the statistics perspective. The prerequisite to realizing this goal is to find a fast, accurate, and non-destructive approach for chiral structure identification. It is worth noting that the CPR method used in Fig. 2d has several limitations, including the requirement of frequent optical path switching (each test point needs to switch the optical path once in order to achieve RCP and LCP light), low characterization efficiency, and difficulty in maintaining the test position precisely unchanged before and after optical path switching. Therefore, the CPR method is not suitable for statistical chirality characterization of a quantity of 2D crystals. We utilized the approach mentioned in Fig. 3h and used the peak intensity ratio between Raman mode III and V (I_{III}/I_V), denoted as the normalized intensity of mode III, to determine the 2D chiral configuration of ReS$_2$ on MgO. This strategy needs no optical path switching and can identify the chirality of each test point by only one spectrum. Figure 3i, j showed the angle-resolved Raman intensities of mode III and mode V under parallel configuration corresponding to one R-ReS$_2$ domain and one S-ReS$_2$ domain grown on MgO(12l)^R and MgO(12l)^S, respectively. It displayed that the double-lobed pattern of mode V (blue) did not change with the variation of the product chirality, manifesting that Raman mode V of ReS$_2$ is insensitive to the product's chirality. On the contrary, the patterns of mode III (red) corresponding to R- and S-ReS$_2$ were mirror symmetric, indicating that the intensity of mode III had a significant dependence on the product's chirality. We measured I_{III}/I_V under $\varphi = 120°$ to determine ReS$_2$ chirality, which is due to the following reasons: (i) Selecting the normalized rather than the absolute intensity of Raman mode III as chirality criterion can avoid the influence of experimental variables unrelated to ReS$_2$ chiral configurations, such as tiny fluctuation of incident laser power and subtle variation of laser focusing degree on different samples. (ii) When $\varphi = 120°$, the I_{III}/I_V corresponding to S- and R-ReS$_2$ reach the maximum and secondary maximum values in their

Fig. 3 | Step-by-step structural selectivity improvement of as-grown ReS₂ by substrate engineering. a–d AFM images showing bare MgO(001) (**a**), and monolayer ReS₂ grown on reconstructed MgO(11*l*) (**b**), MgO(12*l*)^R (**c**), and MgO(12*l*)^S (**d**), respectively. Regions to the left of the white dashed lines in (**b–d**) are monolayer ReS₂-covered MgO surfaces with steps along $[\bar{1}10]$, $[\bar{2}10]$, and $[\bar{1}20]$ marked by white, blue, and red arrows, respectively. Areas to the right of the white lines are bare substrates. The atomic models corresponding to each surface are displayed below the AFM images. Large spheres in different shades of orange represent O atoms in different layers of the MgO substrate, while small gray spheres represent Mg atoms. Scale bars: 200 nm. Insets in (**b–d**) are the nanometer-scale AFM images showing the reconstructed steps and kinks on the corresponding substrates after annealing. The white and yellow dashed lines mark the steps and kinks, respectively. Scale bar: 30 nm. **e** Optical image showing ReS₂ domains grown on MgO(001) with two preferred orientations of 0° and 90°. Scale

bar: 50 μm. The inset is an angle-resolved Raman intensity mapping of mode V for ReS₂ domains grown on MgO(001). Scale bar: 5 μm. **f** Low-energy electron diffraction (LEED) patterns of ReS₂ grown on M**g**O(001). **g** In-plane orientation histograms of ReS₂ domains grown on MgO(001) and MgO(11*l*), respectively. 100 domains were counted on each substrate. **h** Linearly polarized Raman spectra of *R*-ReS₂ and *S*-ReS₂ for a laser wavelength of 532 nm. Inset is an optical image showing that the ***b***-axis of ReS₂ (black arrow) is rotated 120° with respect to the polarization direction of the incident laser (green arrow) during characterization. Scale bar: 5 μm. **i**, **j** Polarization dependence of the intensities of Raman modes III (red) and V (blue) at 151 cm⁻¹ and 212 cm⁻¹ for *R*-ReS₂ (**i**) and *S*-ReS₂ (**j**), respectively. The ***b***-axis of ReS₂ is marked by the black arrow. **k**, **l** Statistical distributions of the normalized intensity of Raman mode III (I_{III}/I_V) for ReS₂ domains grown on MgO(12*l*)^R and MgO(12*l*)^S (insets), respectively. The measurement condition was the same as that in (**h**). Each substrate counted ≈ 200 domains.

polar plots, respectively (Supplementary Fig. 22), implying that the change rates of I_{III}/I_V with φ are minimum at these two points. Therefore, selecting $\varphi = 120°$ helps improve the robustness of the measured I_{III}/I_V even when the true φ values in the experiments slightly deviated from 120°. The normalized mode III intensities of *R*- and *S*-ReS₂ were measured to be 2.2 ± 0.6 and 6.3 ± 1.8, respectively. Polarization-resolved Raman mapping further shows homogeneous I_{III}/I_V distributions within and across crystals, confirming single-crystallinity and uniform chirality (Supplementary Fig. 23). Statistics of I_{III}/I_V corresponding to ~200 ReS₂ crystals grown on MgO(12*l*)^R and MgO(12*l*)^S, showed that *R*-ReS₂ accounted for 97.5% of the total domains on MgO(12*l*)^R (Fig. 3k), and *S*-ReS₂ accounted for 98.7% on MgO(12*l*)^S (Fig. 3l). Apart from the control of chirality, the nucleation density of monolayer ReS₂ single crystals can also be modulated by adjusting the

density of step edges and kinks on the chiral MgO substrate (Supplementary Figs. 24–26).

Device performance of chiral ReS₂ single crystals

We transferred the as-grown ReS₂ on a SiO₂/Si substrate to fabricate a back-gated field effect transistor (FET) with Cr/Au utilized as the contact electrode to achieve matched work function at the interface (Supplementary Fig. 27). The I_{ds}-V_{ds} curve displays linear characteristics, indicating a low-resistance ohmic contact between ReS₂ and the electrode (Supplementary Fig. 28). The transfer curve in Fig. 4a manifests a typical n-type semiconducting behavior. We calculated the carrier mobility ($\mu = \frac{dI_{ds}}{dV_g} \cdot \frac{L}{W} \cdot \frac{1}{C_i \cdot V_{ds}}$, where L and W represent the length and width of the FET device, and $C_i = 12.1$ nF cm⁻² is the measured
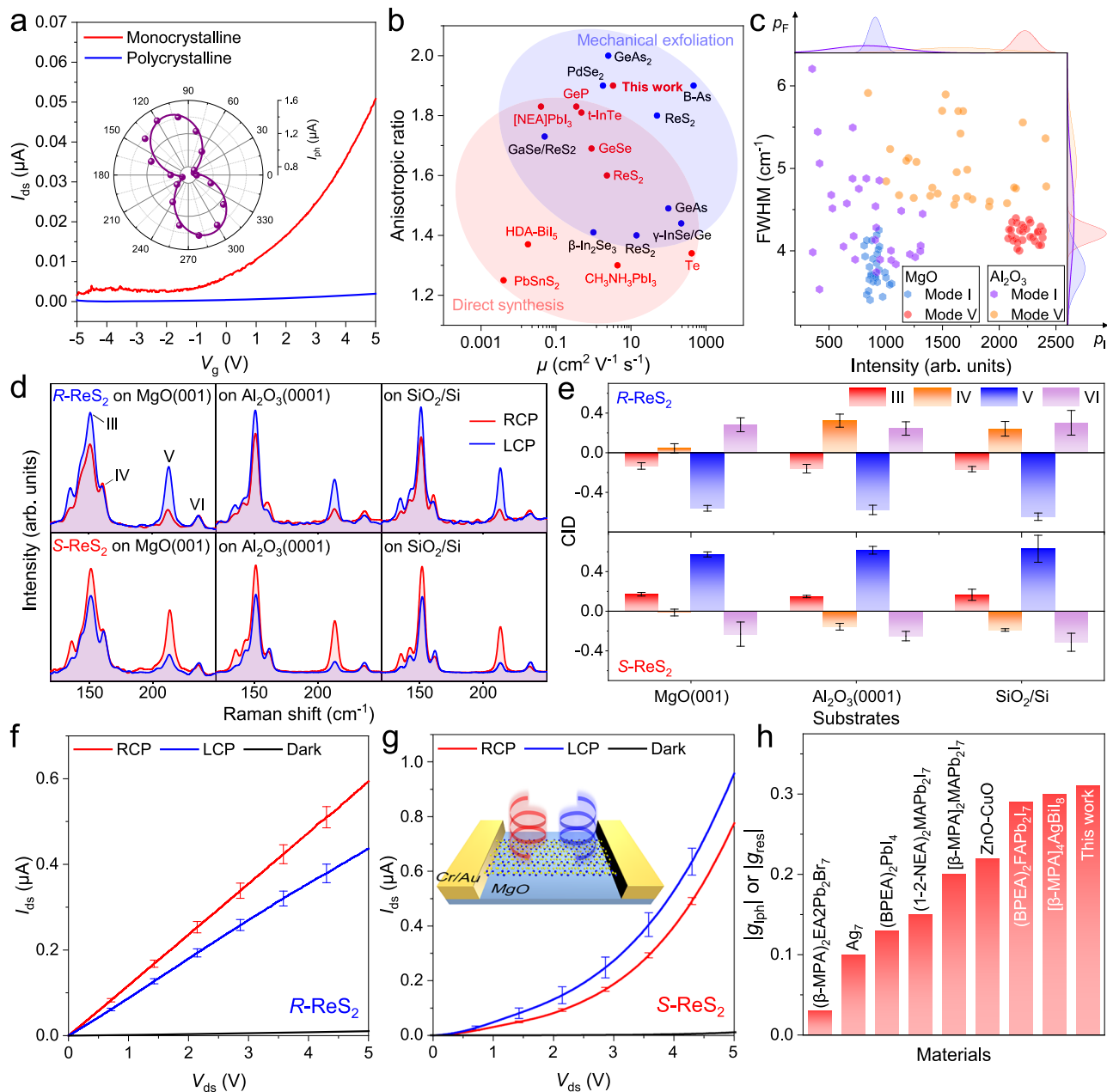
Fig. 4 | Electrical and photoelectric properties of chiral monolayer ReS₂ single crystals. a I_{ds}-V_g curves of single-crystalline and polycrystalline monolayer ReS₂-based field effect transistor (FET) devices. Here, I_{ds} denotes the drain-source current, and V_g is the gate voltage. The channel length/width ratios (L/W) are 2.57 and 2.49 for the single- and poly-crystalline devices, respectively. Inset is the linear polarization-dependent photocurrent of the single-crystalline device under 532 nm laser illumination. **b** Carrier mobility *vs.* anisotropic ratio in photodetection of various 2D low-symmetry materials to compare our ReS₂ device performance with the other state-of-the-art devices (Supplementary Table 1). **c** Statistical distributions of full width at half maximum (FWHM) and intensities corresponding to Raman mode I and V for ReS₂ single crystals grown on chiral MgO and polycrystals grown on α-Al₂O₃. Each substrate counted 30 domains. **d** CPR spectra for *R*- and *S*-ReS₂ transferred onto the MgO(001), α-Al₂O₃(0001), and SiO₂/Si substrate, respectively. **e** CID values for *R*- and *S*-ReS₂ on MgO(001), α-Al₂O₃(0001), and SiO₂/Si. Each substrate counted 20 domains. Error bars are standard deviations. **f, g** I_{ds}-V_{ds} curves of *R*- and *S*-ReS₂-based photodetectors under 532 nm circularly polarized light (CPL) illumination. Error bars represent the standard deviation from several measurements. **h** Comparison of the asymmetrical factor for photocurrent between our monolayer chiral single-crystalline ReS₂-based photodetector for CPL detection and the other state-of-the-art low-symmetry 2D material-based devices (Supplementary Table 2).

capacitance per unit area for 285 nm SiO₂ layer), yielding $\mu = 3.35\ cm^2\,V^{-1}\,s^{-1}$ for the single-crystalline ReS₂ grown on MgO(12*l*)^R at room temperature, which is among the highest reported for CVD-grown ReS₂ and is 30 times higher than that of polycrystalline ReS₂ prepared on α-Al₂O₃(0001) (0.11 cm² V⁻¹ s⁻¹). The transconductance ($g_m = \frac{dI_{ds}}{dV_g}$) extracted from the linearly region of the transfer curve is 0.35 μA/V, comparable to those of mechanically exfoliated ReS₂[39,40].

Monolayer ReS₂ can produce anisotropic photoresponse in the visible band due to its low lattice symmetry and direct bandgap of 1.43 eV[41] (Supplementary Fig. 29). Under 532 nm laser illumination, the responsivity of the single-crystalline ReS₂ device ($R = \frac{I_{ph}}{P}$, where I_{ph} is the photocurrent and P is the light power) was 113.76 A W⁻¹ at zero gate voltage ($V_g = 0$) and a low bias voltage ($V_{ds} = 0.1\ V$), whose performance is in the first echelon among the CVD-prepared 2D anisotropic materials under similar measurement conditions. More importantly, the

photocurrent of the ReS₂ device showed prominent dependence on the linear polarization direction of the incident light under the bias voltage ranging from 0 to 2 V (Supplementary Fig. 30), yielding a superior anisotropic ratio of 1.9 when $V_{ds} = 1.7$ V (inset of Fig. 4a). The photocurrent reached maximum when the laser polarization direction was parallel to the **b**-axis of ReS₂. Both the optical anisotropic ratio and the carrier mobility of our single-crystalline ReS₂-fabricated device are among the highest values reported for CVD-grown ReS₂ to date and are comparable to those of many mechanically exfoliated anisotropic 2D materials with larger thickness (Fig. 4b).

We further verified the crystal quality by the in-plane (mode I at 131 cm⁻¹) and out-of-plane (mode V at 212 cm⁻¹) Raman vibrational modes to unclose the excellence reason of our sample in some electrical and photoelectric performances. Statistics show that single-crystalline ReS₂ grown on MgO(12*l*)^R exhibits remarkably narrower distributions of full width at half maximum (FWHM) and more uniform Raman peak intensities for both mode I and V compared with the polycrystalline counterparts prepared on α-Al₂O₃(0001) (Fig. 4c). The FWHM and peak intensity variances of the single-crystalline samples are only ~30% and ~20% of those of the polycrystalline specimens (Supplementary Fig. 31), indicating high and homogeneous crystal quality.

Next, we investigated the 2D chiral structure-related physical properties and device performances of as-grown ReS₂. We transferred monolayer *R*-and *S*-ReS₂ grown on MgO(12*l*)^R and MgO(12*l*)^S to three achiral substrate surfaces with different chemical compositions and structures, which are MgO(001), α-Al₂O₃(0001) and the amorphous SiO₂/Si. The ReS₂ enantiomers displayed obvious helicity-dependent Raman intensities on all three substrates, and the *R*- and *S*-ReS₂ showed opposite chiral Raman responses, indicating that the 2D chirality of monolayer ReS₂ is predominantly determined by its out-of-plane orientation and is independent of whether the substrate surface is chiral or not (Fig. 4d, e). These results validate a universal and robust strategy to construct 2D chiral interfaces on diversified substrates using atomically thin low-symmetry materials. The CID values of *R*-ReS₂ on the three substrates excited by LCP are higher than those by RCP for mode III (153 cm⁻¹) and V (212 cm⁻¹), while mode IV (162 cm⁻¹) and VI (235 cm⁻¹) display opposite chiral Raman responses. *S*-ReS₂ behaved the opposite. In addition, the CID values for the same Raman mode of ReS₂ on different substrates vary slightly, which may stem from different electron-photon and electron-phonon interactions in ReS₂ due to disparate charge transfer between ReS₂ and the substrate and the intrinsic optical property disparity of various substrates[25,42,43].

The CPL detection ability of our chiral monolayer ReS₂ was then studied by fabricating a photodetector directly on the MgO substrate in order to eliminate the negative impact on the device performance from the contamination introduced in the transfer procedure. The *R*-ReS₂ device displayed a larger photocurrent under 532 nm RCP illumination than under the LCP illumination, while the *S*-ReS₂ device behaved the opposite, demonstrating prominent CPL distinguishability (Fig. 4f, g). We quantified the distinguishability of CPL detection by an asymmetrical factor for photocurrent ($g_{Iph} = \frac{2(I_{LCP} - I_{RCP})}{I_{LCP} + I_{RCP}}$, where I_{LCP} and I_{RCP} are the photocurrent under LCP and RCL irradiation) and yielded g_{Iph} of −0.31 and 0.20 for *R*-ReS₂ and *S*-ReS₂, respectively, which are comparable to those chiral perovskites and metal oxides with larger thickness (Fig. 4h and Supplementary Table 2).

Discussion

We demonstrate a terrace-step-kink strategy for the direct growth of single-chirality, unidirectional, semiconducting, anisotropic monolayer ReS₂ single crystals on the custom-designed chiral surface of insulating MgO, yielding >99% in-plane orientation consistency and >97.5% chirality selectivity. Our combined experimental and theoretical results show that terrace facets determine the epitaxial direction of ReS₂ while steps and kinks break the configuration and energy degeneracy of ReS₂ in the lateral orientation and chirality. The as-

grown products can be facilely transferred to various substrates and robustly construct chiral interfaces. The high quality of monolayer ReS₂ is further evidenced by the large carrier mobility, superior anisotropic ratio in photoresponse (1.9) comparable to mechanically exfoliated samples, and high distinguishability of CPL comparable to those typical chiral materials with larger thickness. The terrace-step-kink strategy is applicable to the chiral epitaxy of other low-symmetry 2D single crystals, like monoclinic MoO₂. This work extends the range of control over 2D material growth to chirality, demonstrating full manipulation of both in-plane and out-of-plane lattice orientations of 2D crystals via the synergy of terraces, steps, and kinks on the substrate and enabling chirality transfer from the substrate to the 2D materials. Our findings offer the opportunity to produce wafer-scale, chirality-selective, single-crystalline ReS₂ membranes and have the potential to be generalized to other low-symmetry 2D crystals.

Methods

Annealing of MgO substrate

Single-side polished MgO substrates were purchased from Hefei Ruijing Photoelectric Technology Co. To reconstruct terraces, steps, and kinks on the surface, the MgO substrates were annealed in an oxygen atmosphere at 1050 °C for approximately 2 h.

Growth and transfer of ReS₂ domains

A 0.0025 mol/L aqueous solution of NaReO₄ was prepared by dissolving NaReO₄ in deionized water. Single-side polished c-plane sapphire were treated with oxygen plasma to create a hydrophilic surface. The prepared salt solution was spin-coated onto the plasma-treated sapphire surface at 5000 rpm for 30 s, which was then used to provide precursor vapor to the target substrate for ReS₂ growth. The growth process was carried out in a 1-inch diameter atmospheric pressure CVD system. During growth, sulfur powder was placed in an Al₂O₃ crucible and positioned at the center of the low-temperature zone, with the temperature set to 140−180 °C. The MgO substrate or other substrates were placed face-to-face on the sapphire substrate spin-coated by NaReO₄ solution to form a spatially confined reaction microchamber, which was positioned at the center of the high-temperature zone (820−880 °C). For the growth of monolayer ReS₂ domains, 50 sccm of high-purity Ar was used as a carrier gas, and growth was conducted for 10−20 min (Supplementary Fig. 32).

The transfer of ReS₂ domains was conducted using a polymer-assisted method. A thin film of poly (methyl methacrylate) (PMMA) was spin-coated onto the ReS₂/substrate surface. The sample was then floated on a 2 mol/L potassium hydroxide (KOH) solution, allowing the PMMA/ReS₂ film to gently detach from the substrate. The detached film was rinsed in deionized water three times to remove residual etchants. The PMMA/ReS₂ film was subsequently transferred onto a TEM grid or other substrates, naturally dried in air, and baked on a hotplate at 180 °C for 15 min. To remove the PMMA, the sample was immersed in acetone for 8 h.

Characterization

(i). **Optical characterization**. Optical images were captured using an Olympus BX53M microscope. Raman spectra were acquired using a Renishaw Qontor confocal Raman spectrometer with a 532 nm excitation laser. The laser was focused, and scattered light was collected through either a 100× or 50× Leica objective lens. A grating of 1800 lines/mm was used for spectral acquisition. All linearly polarized Raman measurements were conducted in a parallel polarization configuration, where the analyzer was aligned parallel to the incident polarization direction. The CPR spectra were obtained by inserting a quarter-wave plate into the light path. SHG measurements were carried out using a micro-spectral scanning system (MStarter 100) with a 1064 nm laser.

(ii). **Top-view STEM characterization**. ADF-STEM imaging in Fig. 2b was performed at room temperature using an aberration-corrected Titan Cubed Themis G2 300 microscope. The STEM was operated under an accelerating voltage of 300 kV, with a condenser lens aperture of 50 mm, a convergence semi-angle of 21.3 mrad, and a collection angle of 39–200 mrad. The dwell time for a single frame was set to 2 μs per pixel, with a pixel size of 0.012 nm px^{-1} and a beam current of 30 pA. Image processing was conducted using ImageJ software. A Gaussian blur filter (≈ 2 pixels) was applied to high-magnification ADF-STEM images for smoothing. To enhance visualization, false color LUT was applied to some grayscale ADF-STEM images. Atomic models were constructed using the Accelrys Discovery Studio Visualizer and VESTA[44] software.

(iii). **Cross-sectional STEM characterization**. A dual-beam focused ion beam (FIB) system (Thermo Scientific Scios 2) was employed for sample preparation. Initially, a 200-nm carbon protective layer was deposited using e-beam deposition within the FIB system. The sample was then tilted perpendicular to the ion beam, after which a tungsten strap layer (2 μm) was deposited to shield the region of interest during the milling process. A Ga+ ion beam was utilized to thin and purge the sample to a final thickness of 50 nm for subsequent analysis. For in-plane STEM investigations, the prepared samples were transferred onto TEM grids via a wet-transfer method, and the experiments were conducted using a JEOL GrandARM300F at an accelerating voltage of 300 kV. In STEM imaging, the electron beam was focused to <0.1 nm, using a semi-convergence angle of approximately 24 mrad and a 30 μm condenser lens aperture.

(iv). **SEM and AFM characterization**. SEM images were obtained using Regulus 8100 system at 3 kV, 10 μA. AFM measurements were performed by an Asylum Cypher S system. Oxford (AC200TS) Al(100)-coated silicon cantilevers were used. The resonance frequency was ~150 kHz. The spring constant was ~9 N m^{-1} and the tip curvature radius was ~7 nm.

(v). **XRD, SAED, and LEED characterization**. XRD measurements were conducted using multipurpose X-ray diffractometer (SmaterLab SE) with a copper target. SAED patterns were obtained using transmission electron microscopy (JEOL F200). LEED (OCI, LEED 450) were performed under an ultrahigh vacuum at room temperature.

(vi). **Device fabrications and measurements**. The ReS$_2$ domains grown on MgO and α-Al$_2$O$_3$ substrates were transferred onto SiO$_2$/Si (285 nm) substrates for the fabrication of FETs (Fig. 4a), while photodetectors (Fig. 4f, g) were fabricated directly on the chiral MgO substrates. Both FETs and photodetectors were constructed using a photolithographic pattern transfer technique. Electrodes (10 nm Cr/40 nm Au) were deposited on the substrate through standard photolithography, followed by thermal evaporation and a lift-off process. The prepared electrodes were then transferred onto the target sample using the aligned dry-transfer method. Electronic and optoelectronic measurements were performed on a probe station using a semiconductor device analyzer (Keithley 2612B). A linearly polarized beam (532 nm) with a defined polarization direction was focused onto the device through a 50× objective, with its intensity calibrated using a standard optical power meter (Thorlabs PM100D). CPL was generated using a quarter-wave plate (KungXuan K0.A225.532). All measurements were conducted in the air at room temperature.

DFT calculations

DFT calculations were performed using the plane-wave method implemented in the Vienna Ab initio Simulation Package[45,46]. The projected augmented wave pseudo-potentials[47], the Perdew-Burke-Ernzerh exchange-correlation functional were adopted in all the calculations[48]. The energy cutoff was set as 400 eV for the plane-wave basis set for the sake of high accuracy. A vacuum layer of 20 Å was used to avoid the interference of the adjacent periodic images. For supercells featuring distinct geometries or sizes, Monkhorst−Pack k-point sampling was implemented with a grid spacing of ∼ 0.03 Å^{-1} along each reciprocal lattice vector within the Brillouin zone. The energy and force convergence criteria were set to 10^{-4} eV and 0.01 eV/Å, respectively.

We constructed the ReS$_2$-MgO(001) heterojunction with orientations varying by intervals of 15°(Supplementary Fig. 33 and Supplementary Table 3). The 0° orientation corresponds to the configuration where the **b**-axis of ReS$_2$ is aligned parallel to the MgO[110] direction. The binding energies were calculated as

$$E_b = \left(E_{\mathrm{ReS_2-MgO(001)}} - E_{\mathrm{ReS_2}} - E_{\mathrm{MgO(001)}} \right)/S \qquad (1)$$

where the $E_{\mathrm{ReS_2-MgO(001)}}, E_{\mathrm{ReS_2}}, E_{\mathrm{MgO(001)}}$ represent the total energy of ReS$_2$ on MgO(001) substrate and the energy of isolated ReS$_2$ and MgO(001) substrate, respectively. S indicates the contacting area between ReS$_2$ and MgO(001) substrate. Then, we compared the grain boundary formation energies of 90° and 45° GBs using the following formula:

$$E_f = E_{tot} - xE(\mathrm{ReS_2}) \qquad (2)$$

where E_{tot} is the total energy of the ReS$_2$ with GBs, $E(\mathrm{ReS_2})$ is the energy of ReS$_2$ per unit (each unit here has one Re and two S atoms), x is the total number of Re atoms (number of units) in the structure of ReS$_2$ with GBs.

Next, we built a ReS$_2$-MgO(11l) heterojunction featuring step $[\bar{1}10]$ (Supplementary Fig. 34 and Supplementary Table 4). We compared the binding energies between two orientations where the **b**-axis in ReS$_2$ aligns parallel or perpendicular to the step $[\bar{1}10]$. The binding energies were calculated as

$$E_b = \left(E_{\mathrm{ReS_2-MgO(11l)}} - E_{\mathrm{ReS_2}} - E_{\mathrm{MgO(11l)}} \right)/2L \qquad (3)$$

where $E_{\mathrm{ReS_2-MgO(11l)}}, E_{\mathrm{ReS_2}}$, and $E_{\mathrm{MgO(11l)}}$ represent the total energy of ReS$_2$ on the MgO(11l) substrate, the energy of isolated ReS$_2$, and the energy of the MgO(11l) substrate, respectively. L indicates the length along the step $[\bar{1}10]$.

Finally, we constructed ReS$_2$-chiral MgO heterojunction, introducing both step $[\bar{1}10]$ and kink $[\bar{1}00]$, (Supplementary Fig. 35 and Supplementary Table 5). We compared the binding energies of ReS$_2$ with different chirality on the chiral MgO surface, using the formula:

$$E_b = \left(E_{\mathrm{ReS_2-chiral\ MgO}} - E_{\mathrm{ReS_2}} - E_{\mathrm{chiral\ MgO}} \right)/S \qquad (4)$$

where the $E_{\mathrm{ReS_2-chiral\ MgO}}, E_{\mathrm{ReS_2}}, E_{\mathrm{chiral\ MgO}}$ represent the total energy of ReS$_2$ on chiral MgO substrate, the energy of isolated ReS$_2$ and the energy of chiral MgO substrate, respectively. S denotes the contact area between ReS$_2$ and chiral MgO substrate.

Data availability

Relevant data supporting the key findings of this study are available within the article and the Supplementary Information file. All raw data generated during the current study are available from the corresponding authors upon request.

References

1. Liu, Y. et al. Promises and prospects of two-dimensional transistors. *Nature* **591**, 43–53 (2021).
2. Das, S. et al. Transistors based on two-dimensional materials for future integrated circuits. *Nat. Electron.* **4**, 786–799 (2021).

3. Akinwande, D. et al. Graphene and two-dimensional materials for silicon technology. *Nature* **573**, 507–518 (2019).

4. Wang, Q. H., Kalantar-Zadeh, K., Kis, A., Coleman, J. N. & Strano, M. S. Electronics and optoelectronics of two-dimensional transition metal dichalcogenides. *Nat. Nanotechnol.* **7**, 699–712 (2012).

5. Wang, J. et al. Dual-coupling-guided epitaxial growth of wafer-scale single-crystal WS_2 monolayer on vicinal a-plane sapphire. *Nat. Nanotechnol.* **17**, 33–38 (2022).

6. Zhu, H. et al. Step engineering for nucleation and domain orientation control in WSe_2 epitaxy on c-plane sapphire. *Nat. Nanotechnol.* **18**, 1295–1302 (2023).

7. Zheng, P. et al. Universal epitaxy of non-centrosymmetric two-dimensional single-crystal metal dichalcogenides. *Nat. Commun.* **14**, 592 (2023).

8. Li, T. et al. Epitaxial growth of wafer-scale molybdenum disulfide semiconductor single crystals on sapphire. *Nat. Nanotechnol.* **16**, 1201–1207 (2021).

9. Hu, J. et al. Epitaxial growth of high-quality monolayer MoS_2 single crystals on low-symmetry vicinal Au(101) facets with different Miller indices. *ACS Nano* **17**, 312–321 (2023).

10. Zhang, F. et al. Full orientation control of epitaxial MoS_2 on hBN assisted by substrate defects. *Phys. Rev. B* **99**, 155430 (2019).

11. Zhang, X. et al. Defect-controlled nucleation and orientation of WSe_2 on hBN: a route to single-crystal epitaxial monolayers. *ACS Nano* **13**, 3341–3352 (2019).

12. Aljarb, A. et al. Interfacial reconstructed layer controls the orientation of monolayer transition-metal dichalcogenides. *ACS Nano* **17**, 10010–10018 (2023).

13. Li, L. et al. Epitaxy of wafer-scale single-crystal MoS_2 monolayer via buffer layer control. *Nat. Commun.* **15**, 1825 (2024).

14. Lee, J. H. et al. Wafer-scale growth of single-crystal monolayer graphene on reusable hydrogen-terminated germanium. *Science* **344**, 286–289 (2014).

15. Xu, X. et al. Ultrafast epitaxial growth of metre-sized single-crystal graphene on industrial Cu foil. *Sci. Bull.* **62**, 1074–1080 (2017).

16. Si, K. et al. Quasi-equilibrium growth of inch-scale single-crystal monolayer α-In_2Se_3 on fluor-phlogopite. *Nat. Commun.* **15**, 7471 (2024).

17. Wang, L. et al. Bevel-edge epitaxy of ferroelectric rhombohedral boron nitride single crystal. *Nature* **629**, 74–79 (2024).

18. Qin, B. et al. Interfacial epitaxy of multilayer rhombohedral transition-metal dichalcogenide single crystals. *Science* **385**, 99–104 (2024).

19. Chang, C. et al. Remote epitaxy of single-crystal rhombohedral WS_2 bilayers. *Nat. Commun.* **15**, 4130 (2024).

20. Yang, Y. et al. Controllable growth of type-II Dirac semimetal $PtTe_2$ atomic layer on Au substrate for sensitive room temperature terahertz photodetection. *Info.Mat* **3**, 705–715 (2021).

21. Wu, D. et al. Unidirectional growth of molybdenum dioxide nanoflakes on C-sapphire substrate via buffer layer induction. *Mater. Charact.* **216**, 114307 (2024).

22. Tan, C. et al. Wafer-scale growth of single-crystal 2D semiconductor on perovskite oxides for high-performance transistors. *Nano Lett.* **19**, 2148–2153 (2019).

23. Li, X. et al. Realizing the intrinsic anisotropic growth of 1T' ReS_2 on selected Au(101) substrate toward large-scale single crystal fabrication. *Adv. Funct. Mater.* **31**, 2102138 (2021).

24. Chen, H. et al. Large-area aligned growth of low-symmetry 2D ReS_2 on a high-symmetry surface. *ACS Nano* **18**, 35029–35038 (2024).

25. Zhang, S. et al. Quantum interference directed chiral Raman scattering in two-dimensional enantiomers. *Nat. Commun.* **13**, 1254 (2022).

26. Zhang, S. et al. Anomalous polarized Raman scattering and large circular intensity differential in layered triclinic ReS_2. *ACS Nano* **11**, 10366–10372 (2017).

27. Hu, G. et al. Topological polaritons and photonic magic angles in twisted α-MoO_3 bilayers. *Nature* **582**, 209–213 (2020).

28. Liao, M. et al. Precise control of the interlayer twist angle in large scale MoS_2 homostructures. *Nat. Commun.* **11**, 2153 (2020).

29. Zhu, H. & Yakobson, B. I. Creating chirality in the nearly two dimensions. *Nat. Mater.* **23**, 316–322 (2024).

30. Huang, T. et al. Observation of chiral and slow plasmons in twisted bilayer graphene. *Nature* **605**, 63–68 (2022).

31. Qian, Q. et al. Chiral molecular intercalation superlattices. *Nature* **606**, 902–908 (2022).

32. Kim, H. et al. Giant chiral amplification of chiral 2D perovskites via dynamic crystal reconstruction. *Sci. Adv.* **10**, eado5942 (2024).

33. Zhang, R. et al. Efficient quasi-2D perovskite spin light-emitting diodes based on chiral-induced spin selectivity. *Chem. Mater.* **36**, 3812–3819 (2024).

34. Hejazi, K., Luo, Z.-X. & Balents, L. Noncollinear phases in moiré magnets. *Proc. Natl. Acad. Sci. USA* **117**, 10721–10726 (2020).

35. Wu, B. et al. Evidence for moiré intralayer excitons in twisted WSe_2/WSe_2 homobilayer superlattices. *Light Sci. Appl.* **11**, 166 (2022).

36. He, Q. et al. Deeply exploring anisotropic evolution toward large-scale growth of monolayer ReS_2. *ACS Appl. Mater. Interfaces* **12**, 2862–2870 (2020).

37. Huang, L. et al. Mechanical origin of martensite-like structures in two-dimensional ReS_2. *Commun. Mater.* **2**, 87 (2021).

38. Li, X. et al. Nanoassembly growth model for subdomain and grain boundary formation in 1T' layered ReS_2. *Adv. Funct. Mater.* **29**, 1906385 (2019).

39. Kim, S. Y. et al. Drain induced barrier increasing in multilayer ReS_2. *2D Mater.* **7**, 031004 (2020).

40. Lee, B. C. et al. Probing distinctive electron conduction in multilayer rhenium disulfide. *Adv. Mater.* **31**, 1805860 (2019).

41. Tongay, S. et al. Monolayer behaviour in bulk ReS_2 due to electronic and vibrational decoupling. *Nat. Commun.* **5**, 3252 (2014).

42. Buscema, M., Steele, G. A., van der Zant, H. S. J. & Castellanos-Gomez, A. The effect of the substrate on the Raman and photoluminescence emission of single-layer MoS_2. *Nano Res.* **7**, 561–571 (2014).

43. Cong, S., Liu, X., Jiang, Y., Zhang, W. & Zhao, Z. Surface enhanced Raman scattering revealed by interfacial charge-transfer transitions. *Innovation* **1**, 100051 (2020).

44. Momma, K. & Izumi, F. VESTA 3 for three-dimensional visualization of crystal, volumetric and morphology data. *J. Appl. Crystallogr.* **44**, 1272–1276 (2011).

45. Kresse, G. & Furthmüller, J. Efficient iterative schemes for ab initio total-energy calculations using a plane-wave basis set. *Phys. Rev. B* **54**, 11169–11186 (1996).

46. Kresse, G. & Furthmüller, J. Efficiency of ab-initio total energy calculations for metals and semiconductors using a plane-wave basis set. *Comput. Mater. Sci.* **6**, 15–50 (1996).

47. Blöchl, P. E. Projector augmented-wave method. *Phys. Rev. B* **50**, 17953–17979 (1994).

48. Perdew, J. P., Burke, K. & Ernzerhof, M. Generalized gradient approximation made simple. *Phys. Rev. Lett.* **77**, 3865–3868 (1996).

Acknowledgements

Author contributions

S.W. initiated the project and generated experimental protocols. F.D., X.W. and L.D. conducted DFT calculations. Z.W., Y.C. and Y.Y. performed cross-sectional STEM characterization. J.J. grew 2D crystals. D.W. fabricated devices and conducted measurements. X.G., A.L., T.X., H.H., S.Z., Z.L., J.Z. and F.O. discussed the work and gave suggestions. All authors contributed to the data analysis, manuscript writing, and revision of the manuscript.

Competing interests

The authors declare no competing interests.

Additional information

Supplementary information The online version contains supplementary material available at https://doi.org/10.1038/s41467-025-61849-0.

Correspondence and requests for materials should be addressed to Fangping Ouyang, Feng Ding, Zhu-Jun Wang or Shanshan Wang.

Peer review information *Nature Communications* thanks Alessandro Molle and the other, anonymous, reviewers for their contribution to the peer review of this work. A peer review file is available.

Reprints and permissions information is available at http://www.nature.com/reprints

Publisher's note Springer Nature remains neutral with regard to jurisdictional claims in published maps and institutional affiliations.

[1]School of Advanced Materials, Peking University Shenzhen Graduate School, Shenzhen, Guangdong, China. [2]College of Aerospace Science and Engineering, National University of Defense Technology, Changsha, China. [3]School of Physics, Central South University, Changsha, China. [4]Institute of Technology for Carbon Neutrality, Shenzhen Institutes of Advanced Technology, Chinese Academy of Sciences, Shenzhen, China. [5]School of Physical Science and Technology, ShanghaiTech University, Shanghai, China. [6]School of Physics and Technology, Xinjiang University, Urumqi, China. [7]College of Science, National University of Defense Technology, Changsha, China. [8]State Key Laboratory of Powder Metallurgy, and Powder Metallurgy Research Institute, Central South University, Changsha, China. [9]Faculty of Materials Science and Energy Engineering, Shenzhen University of Advanced Technology, Shenzhen, China. [10]Suzhou Laboratory, Suzhou, China. [11]Guangdong Provincial Key Laboratory of Nano-Micro Materials Research, Peking University Shenzhen Graduate School, Shenzhen, China. [12]These authors contributed equally: Junjie Jiang, Xiao Wang, Danyang Wang. ✉e-mail: oyfp@csu.edu.cn; f.ding@siat.ac.cn; wangzhj3@shanghaitech.edu.cn; wangshanshan08@nudt.edu.cn